RSC Advances

PAPER

View Article Online
View Journal | View Issue

Cite this: *RSC Adv.*, 2018, **8**, 26978

Fast removal of methylene blue from aqueous solution using coal-based activated carbon

Taoxia Niu, Jiawei Zhou, Chao Zhang and Shuang Li*

Coal-based activated carbons (CACs) were prepared from three long flame coals with different ash and volatile matter content. CACs prepared by coal with high ash (6.74%) and volatile matter content (34.31%) showed better adsorption efficiency towards MB (547.35 mg g^{-1}) due to higher surface area and pore volume. The effect of coal to activating agent ratio (CAR) was also investigated in a batch reactor. The porosity development is closely related to the CAR. The calculated monolayer adsorption amount (714.29 mg g^{-1}) was found on YLC-AC-3 with a surface area of 1212.50 m^2 g^{-1}. The equilibrium data were favorably described by the Langmuir and Freundlich isotherm models, and adsorption kinetics fitted well to the pseudo-second order model. The removal efficiency remains at 98.21% after five runs. The results of the present study suggest that CACs are potential and effective adsorbents in fast removal of dyes from aqueous solution.

Received 23rd May 2018
Accepted 23rd July 2018

DOI: 10.1039/c8ra04396e

rsc.li/rsc-advances

1. Introduction

Nowadays, organic dyes are widely used in many industries such as textiles, leather, paper, wool, printing and cosmetics.[1] Large amounts of wastewater containing complex dyes are generated during the coloring process from industries, causing severe environmental problems due to the toxic and carcinogenic effects on living creatures.[2,3] Thus, great attention has been paid to develop an effective method to remove dyes from wastewater efficiently. Methylene blue (MB), as shown in Fig. 1, a stable cationic dye, is difficult to decolorize due to its complex structure and stable chemical properties.[4] However, MB is widely used in the dyeing industry and could cause permanent injury to the eyes of humans and animals.[5]

Various physical and chemical methods, including adsorption, filtration, ion-exchange, ozonation and oxidation have been employed to remove dyes from wastewater.[6] Many disadvantages are coupled with most of these methods. Typically, oxidation method requires high energy costs and will produce by-products. The ion-exchange method has the problems of adsorbent regeneration and disposal requirements. The coagulation/flocculation method will cause high sludge production and formation of large particles. The halflife in the ozonation method is short and the membrane filtration method will produce concentrated sludge.[7] Due to the high efficiency, simplicity of design and flexibility in operation, adsorption is one of the most economical and effective techniques.[8] Various adsorbents have been reported to remove dyes from wastewater, among which, activated carbons (ACs) are most widely used because of their high adsorption capacity, extremely large surface area, micropore volumes and high surface reactivity.[9,10]

ACs could be obtained from various sources of raw materials, such as coal, petroleum, wood, and agricultural wastes. Owning to the advantages of its low cost, and relatively abundant resources, coal is one of the most commonly used precursor for ACs production.[11] Meanwhile, the unique properties, such as well-developed surface area, high mechanical and chemical resistance and easy degradation, coal is sometimes much better than those of synthetic and mineral substances.[12] Thus, coal has been widely selected as a stable alternative precursor for ACs preparation. El Qada and his co-workers reported that AC produced from steam activated bituminous coal showed a equilibrium adsorption capacity of 580 mg g^{-1} for MB.[13] Gao *et al.* prepared a magnetic CAC using bituminous coal in the presence of Fe_2O_3 which exhibited a capacity of 871 mg g^{-1} in MB adsorption at optimized conditions.[14] Duan *et al.* regenerated the spent CAC with a adsorption capacity of 375.93 mg g^{-1} for MB.[15] Li *et al.* found that AC prepared from anthracite through microwave assisted activation could obtain a capacity of 132.03 mg g^{-1} for MB.[16]

Chemical activation is widely used for the preparation of ACs. The broadly used activating agents are KOH, H_3PO_4, $ZnCl_2$,

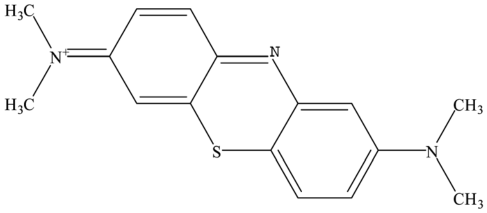

Fig. 1 The molecular structure of MB.

School of Chemical Engineering, Northwest University, Xi'an, Shaanxi 710069, People's Republic of China. E-mail: shuangli722@126.com; Tel: +86-029-88302632

NaOH and K_2CO_3. Jibril *et al.* found AC prepared using KOH as activating agent led to higher surface area, more porous structure with wider pore size distributions than that of H_3PO_4.[17] Gao and co-workers studied the effect of different activating agents in preparation of AC from crab shell, AC activated by KOH exhibited high surface area of 2197 $m^2\ g^{-1}$.[18] Kopac *et al.* prepared two samples using Zonguldak region coal, and found that the samples activated by KOH showed better color removal performance than commercial AC and the sample activated by physical method.[19] According to the previous reports, KOH is the one of the most commonly used activating agent. KOH activation process mainly involves the redox reaction of potassium, carbon oxidation and additional reactions between the active intermediates and the carbon surface, which could produce gas to generate porosity, thus leading to higher surface area, more porous structure with wider pore size distributions.[20] The reactions involved are shown in the following equations:

$$6KOH + C \rightarrow 2K + 3H_2 + 2K_2CO_3 \quad (1)$$

$$K_2CO_3 + C \rightarrow K_2O + 2CO_2 \quad (2)$$

$$2K + CO_2 \rightarrow K_2O + 2CO \quad (3)$$

The main purpose of the present study is to find the relationship between raw coal and the physic-chemical nature of activated carbon materials. The results show that adsorption ability is closely related to the ash and volatile matter content of coal and the CAR. Also, a high MB monolayer adsorption amount (714.29 mg g^{-1}) was recorded on YLC-AC-3 with large surface area (1212.50 $m^2\ g^{-1}$) and pore volume and the optimal CAR is 1 : 3. Adsorption kinetic models and isotherms were also studied in detail.

2. Materials and methods

2.1. Materials

Coals, with size less than 200 mesh (<74 μm), were obtained from different regions of northwestern China, Yulin coal (YLC), Shenfu coal (SFC) and Xinjiang coal (XJC). The raw coals were dried in oven at 393 K for 12 h before used. KOH and ethanol were of analytical grade, and used as received without further purification. MB was supplied by Development of Fine Chemicals of Tianxin (Tianjin, China).

2.2. Preparation of samples

In a typical procedure, coal was pre-carbonized at 723 K for 30 min at a heating rate of 5 K min^{-1}. The obtained char was weighed and then mixed with 6 mol L^{-1} KOH solution under magnetic stir for 2 h at 298 K, and then dried at 333 K for 12 h. Finally, the obtained powder was heated from room temperature to 1073 K at a heating rate of 5 K min^{-1} under 100 mL min^{-1} N_2 flow for 2 h. The resulting samples were washed with deionized water until the filtrate reached neutral. The remaining solid was dried at 393 K for 5 h. The CACs prepared by YLC, SFC and XJC without KOH activation were named as YLC-AC-0, SFC-AC-0 and XJC-AC-0. The prepared CACs using YLC to KOH at mass ratio of 1 : 1, 1 : 2, 1 : 3 and 1 : 4 were named as YLC-AC-1, YLC-AC-2, YLC-AC-3 and YLC-AC-4. Other samples prepared by the same method were named as SFC-AC-1, SFC-AC-2, SFC-AC-3, SFC-AC-4, XJC-AC-1, XJC-AC-2, XJC-AC-3 and XJC-AC-4.

2.3. Characterization

Proximate and ultimate analysis of YLC, SFC and XJC were carried out using an elemental analyzer (VarioEL III , German). The alkali metal and alkaline earth elements analysis (AAEMs) of YLC, SFC and XJC were investigated using an inductively coupled plasma source mass spectrometer (Agilent ICP-OES730). The scanning electron microscopy (SEM) analysis was performed using a scanning electron microscope Carl Zeiss (ZEISS SIGMA). The samples were treated with gold spray before observation. The crystallographic structure was recorded on a diffractometer with Cu Kα radiation ($\lambda = 0.153$ nm), using a X-ray diffractometer (XRD) operated at 40 mA and 40 KV. Data was collected at 0.02° with a rate of 8° min^{-1}, in a 2θ range of 15° to 80°. The surface area and pore structure characteristic were determined by nitrogen adsorption–desorption isotherms at 77 K *via* a Quantachrom NOVA 2200e instrument. The Brunauer–Emmett–Teller (BET) surface area (S_{BET}) and micropore surface area (A_m), micropore volume (V_m) were calculated using the BET equation and *t*-plot method, respectively. Total pore volume (V_t) was calculated by converting the adsorption amount at $P/P_0 = 0.95$ to a volume of liquid adsorbate. All samples were outgassed for 5 h in vacuum at 453 K before measurements. The concentrations of MB were measured by a UV-visible spectrophotometer at the wavelength of maximum absorbance of 664 nm.

2.4. Adsorption experiments of MB

15 mg sample was added to 15 mL MB solution with known concentration and pH value under 300 rpm magnetic stir at 298 K. The samples were taken periodically and centrifuged. The supernatant was collected and the remaining solution was analyzed by a UV-visible spectrophotometer.

The percentage of dye removal efficiency (% Re) and the adsorption capacity (q_t, q_e) were calculated using following equations:

$$\%\ \mathrm{Re} = (C_0 - C_e)/C_0 \times 100 \quad (4)$$

$$q_t = (C_0 - C_t)V/W \quad (5)$$

$$q_e = (C_0 - C_e)V/W \quad (6)$$

Table 1 AAEMs of different coals

	AAEMs (mg kg^{-1}, by dry weight)					
Coal	Ca	Si	Fe	Al	Mg	Na
YLC	21 384.71	655.63	2232.94	933.90	352.62	495.86
SFC	19 402.31	609.29	2395.86	690.11	275.52	374.05
XJC	4428.43	160.59	1458.91	517.30	2223.83	3764.79

Table 2 Proximate and ultimate analysis of different coals

	Proximate analysis (wt%, ad)				Ultimate analysis (wt%, ad)				
Coal	FC_{ad}	M_{ad}	A_{ad}	V_{ad}	C	H	N	S	O
YLC	55.25	3.70	6.74	34.31	70.28	3.87	1.13	0.54	24.18
XJC	54.51	10.07	2.16	33.26	67.83	3.89	0.77	0.10	15.18
SFC	59.93	4.03	4.37	31.67	75.12	4.40	0.94	0.24	10.90

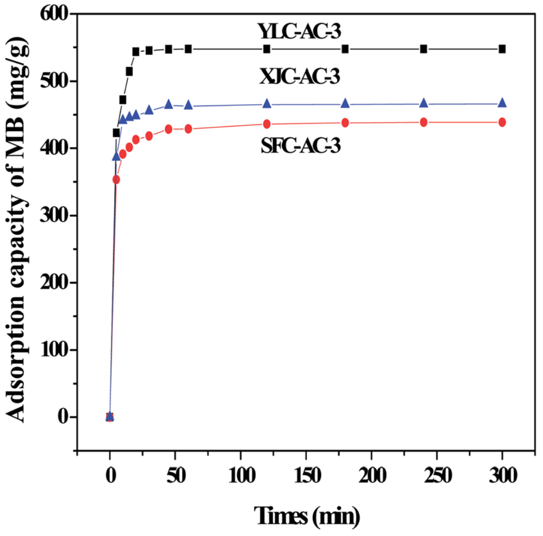

Fig. 2 The adsorption of MB onto different CACs.

where q_e (mg g^{-1}) and q_t (mg g^{-1}) are the adsorption capacity at equilibrium and time t (min), C_0 is the initial concentration of MB (mg L^{-1}), C_e (mg L^{-1}) and C_t (mg L^{-1}) are the concentrations of MB at equilibrium and t (min), respectively, V is the volume of the solution (L), and W is the mass of CACs used (g).

2.5. The regeneration and recycling test

In a typical recycle test, 50 mg sample was added to 50 mL of MB solution with a initial concentration of 100 mg L^{-1}, and the suspension was stirred at 300 rpm for 10 min. The mixture was centrifugated, the supernatant was determined by UV spectrophotometer, the sample dried at 398 K for 5 h and then was calcined at 673 K (5 K min^{-1}) under the N_2 flow rate at 100 mL min^{-1} for 2 h in vertical tube furnace to remove the dye.

3. Results and discussion

3.1. Effects of ash and volatile matter

Porosity development is closed related to ash and volatile matter content. Indeed, minerals (*e.g.* Ca, Si, Fe, Al, Mg, Na) are reported to act as catalyst which accelerate gasification reactions during activation process.[21] Table 1 shows the alkali metal and alkaline earth elements analysis of different coals. The Ca, Si, Fe and Al contents of XJC are the lowest, and Mg and Na contents of XJC are higher than others. The Fe content of YLC is similar to SFC. The Ca, Si and Al contents of YLC are the highest among all the samples.

The evolution of volatiles from the activated carbon favors pore development.[22] To find the relationships between coal reactivity and porosity development, the proximate analysis and ultimate analysis of coals are shown in the Table 2. The volatile matter content decreased in the order of YLC (34.31%) > XJC (33.26%) > SFC (31.67%). Ash content ranged from 6.74% to 2.16% from YLC to XJC. The evolution of CO and CO_2 could generate porosity, therefore a higher oxygen content in raw coal may ensure a higher S_{BET}.[22] A high oxygen content of 24.18% was observed on YLC, and a low oxygen content of 10.9% was found on SFC.

Fig. 2 shows the adsorption of MB onto different CACs. YLC-AC-3 shows a high adsorption amount of 547.35 mg g^{-1} for MB in 20 min, follow by XJC-AC-3 (465.43 mg g^{-1}) and SFC-AC-3 (438.56 mg g^{-1}). As discussed before, the ash and volatile matter content are closely related to porosity, the experimental data follows the same trend. YLC with the highest ash (6.74%), volatile matter content (34.31%) and oxygen content (24.18%) shows the best ability in fast removal of MB.

To further study the effect of ash and volatile matter content of coals on the porosity development of CACs, the samples were characterized by SEM, XRD and N_2 adsorption–desorption.

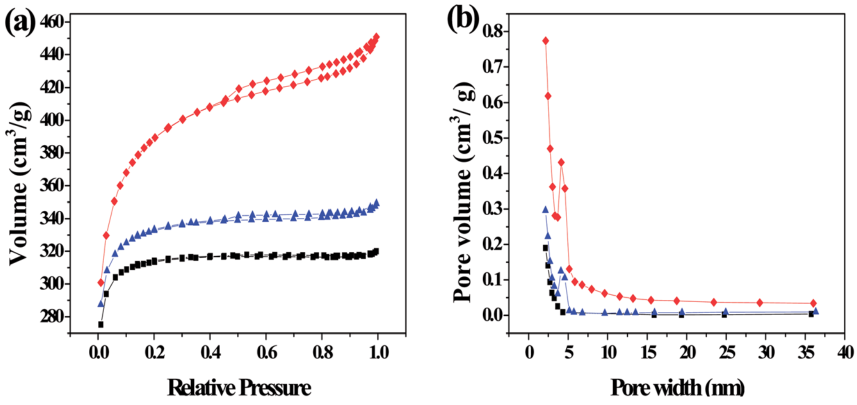

Fig. 3 (a) N_2 adsorption–desorption isotherms and (b) the corresponding pore size distribution (PSD) calculated using adsorption branch of BJH algorithm for samples of YLC-AC-3 (◆), SFC-AC-3 (■) and XJC-AC-3 (▲).

Table 3 Surface area and pore structure of different CACs

Samples	S_{BET} ($m^2\ g^{-1}$)	V_T ($cm^3\ g^{-1}$)	V_m ($cm^3\ g^{-1}$)	S_m ($m^2\ g^{-1}$)	A_{ps} (nm)
YLC-AC-0	26.22	0.01	0.01	13.31	1.49
YLC-AC-3	1212.50	0.69	0.28	613.97	2.26
SFC-AC-0	0.70	0.003	0.003	—	—
SFC-AC-3	942.10	0.49	0.34	643.12	2.09
XJC-AC-0	28.85	0.01	0.01	15.53	1.27
XJC-AC-3	1007.18	0.53	0.34	669.24	2.12

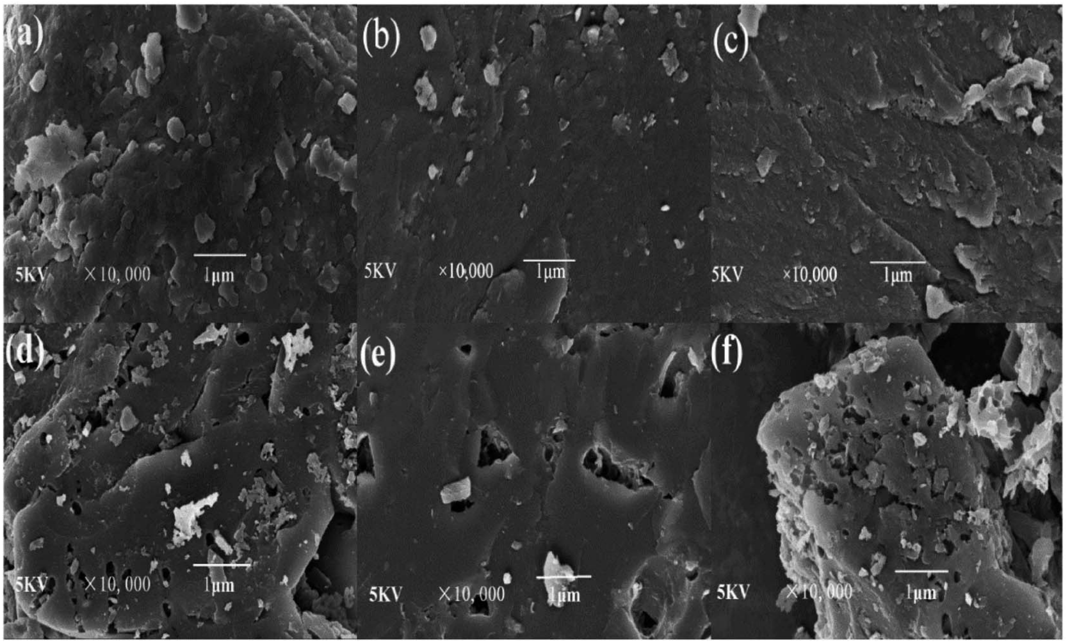

Fig. 4 SEM micrographs of (a) YLC, (b) SFC, (c) XJC, (d) YLC-AC-3, (e) SFC-AC-3, (f) XJC-AC-3 selected at 10 000× magnification.

3.1.1. Porous structure analysis. The nitrogen adsorption–desorption isotherms and pore size distribution are shown in Fig. 3. The isotherms of SFC-AC-3 and XJC-AC-3 demonstrated a rise at low P/P_0 range, and a gradual increase at a relatively high P/P_0 range (Fig. 3), a typical type I isotherm, indicating micropores dominated the materials. The desorption branch shows a small hysteresis loop at relatively high pressure, indicating the existence of mesoporosity. This adsorption behavior suggests a combination of microporous–mesoporous structure.[23] The YLC-AC-3 shows remarkable hysteresis at $P/P_0 > 0.4$, a typical type IV isotherms, indicating the plentiful presence of

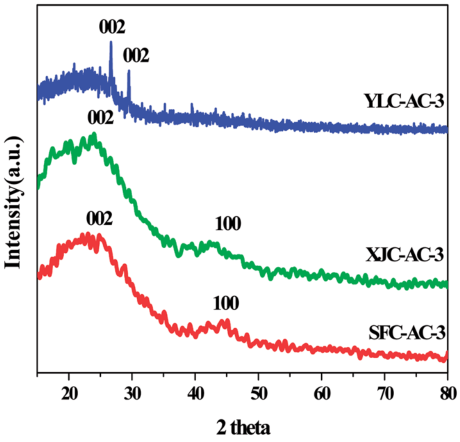

Fig. 5 XRD spectra of YLC-AC-3, SFC-AC-3 and XJC-AC-3.

Table 4 The effect of CAR on MB adsorption amount

Samples	MB adsorption amount ($mg\ g^{-1}$)
YLC-AC-1	445.67
YLC-AC-2	497.47
YLC-AC-3	547.35
YLC-AC-4	532.85
SFC-AC-1	346.22
SFC-AC-2	399.19
SFC-AC-3	438.56
SFC-AC-4	417.33
XJC-AC-1	368.84
XJC-AC-2	418.96
XJC-AC-3	465.43
XJC-AC-4	445.75

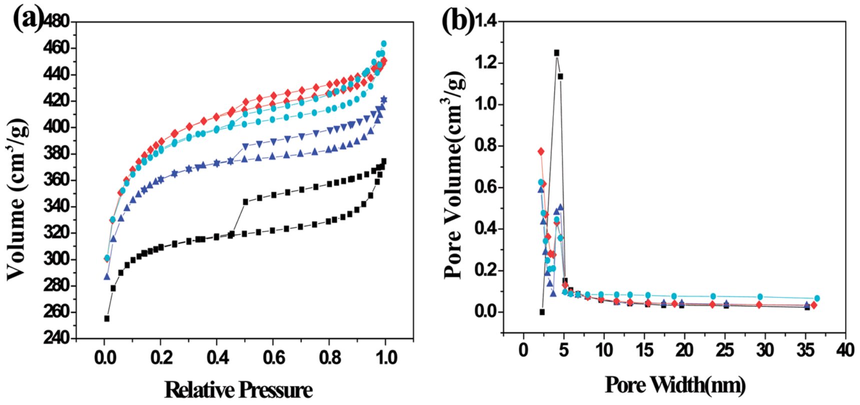

Fig. 6 (a) N_2 adsorption–desorption isotherms and (b) the corresponding pore size distribution (PSD) calculated using adsorption branch of BJH algorithm for samples of YLC-AC-1 (■), YLC-AC-2 (▲), YLC-AC-3 (◆) and YLC-AC-4 (●).

mesopores. The pore size distribution in the range of 2–4 nm further confirmed the mesopores.

Table 3 shows the surface area and pore structure of different CACs. Obviously, KOH activation effectively increased the surface area and pore volume of CACs. The YLC-AC-0, SFC-AC-0 and XJC-AC-0 without KOH activation shows small surface area and pore volume. After KOH activation, the surface area and pore volume of YLC-AC-3, SFC-AC-3 and XJC-AC-3 increased tremendously. The SFC-AC-3 with the relatively low ash and volatile matter content shows the lowest surface area of 942.10 m^2 g^{-1} and pore volume of 0.49 cm^3 g^{-1}, compared with XJC and YLC. On the other hand, a high surface area (1212.50 m^2 g^{-1}) and pore volume (0.69 cm^3 g^{-1}) of YLC-AC-3 was observed, which might be closely related to the minerals in ash and high volatile matter content as discussed in Section 3.1. Porosity development and thus high surface area values are results of pores created by both volatiles evolution and KOH activation. The kinetic diameter of MB molecule is 1.43 × 0.61 × 0.4 nm.[24] These dimensions allow MB to have easy access within the porous structure of CACs, the average pore size are approximately 2 nm. Among the six CACs, the YLC-AC-3 shows the best adsorption capacity of MB due to its large surface, pore volume and relatively larger average pore size.

3.1.2. Surface morphology analysis. The SEM images of different coals and CACs are shown in Fig. 4. It showed that the surfaces of YLC, SFC and XJC are relatively smooth without any pores except for some occasional cracks. After KOH activation, the external surfaces of three CACs all show irregular pores. The surface of YLC-AC-3 (Fig. 4d) is relatively rough and exhibits more pores. While SFC-AC-3 with low ash and volatile matter content shows a fairly smooth surface. Ahmed *et al.* reported that metallic potassium formed during the gasification process could diffuse into the internal structure of carbon matrix widening the existing pores and created new porosities.[25]

3.1.3. Crystal structure. XRD patterns of all samples are shown in Fig. 5. An obvious peak at around 24° and a broad peak at 44° on SFC-AC-3 and XJC-AC-3, could be attributed to the (002) crystal face of graphitic carbon and the (100) reflections of disordered stacking of micrographites. The peaks at around 26° and 29° on YLC-AC-3 corresponded to the (002) reflections of graphitic carbon and the disordered stacking of micrographites (JCPDS no. 41-1487).[11] The diffraction angle of (002) crystal face of SFC-AC-3 and XJC-AC-3 is smaller than YLC-AC-3. From Bragg equation $2dhkl \sin \theta = n\lambda$, the plane spacing *d* (002) of diffraction crystal face (002) for SFC-AC-3 and XJC-AC-3 is relatively large, indicating that the turbostratic degree of the SFC-AC-3 and XJC-AC-3 is apparent.[26]

3.2. Effect of coal to activating agent ratio (CAR)

The CAR plays a key role in development of porosity, including the micropore volume as well as the micropores size distribution.[27,28] Table 4 shows the effect of CAR on MB adsorption amount. The adsorption amount of MB rose from 445.67 mg g^{-1} to 547.35 mg g^{-1}, 346.22 mg g^{-1} to 438.56 mg g^{-1} and 368.84 mg g^{-1} to 465.43 mg g^{-1} when CAR from 1 : 1 to 1 : 3 on YLC-AC, SFC-AC and XJC-AC, respectively. Wu *et al.* reported that increasing KOH amount could enhance the pore development and create new pores during activation process because with the rising ratio, more active sites could react with KOH.[29] The activation reaction was strengthened and a large number of pores were formed with the rising ratio from 1 : 1 to 1 : 3, therefore the adsorption capacity increased due to the larger surface and pore volume. When CAR reached 1 : 3, the carbons on the active sites could be reacted completely, and the adsorption capacity reached the maximum.[30] When CAR reached 1 : 4, the excessive KOH would promote vigorous gasification reaction, which destroys the carbon framework leading to a dramatic decrease of accessible area.[31] Therefore, the adsorption amount of MB decreased. To further study the effect

Table 5 Effect of CAR on pore structure of CACs

Parameters	YLC-AC-1	YLC-AC-2	YLC-AC-3	YLC-AC-4
S_{BET} (m^2 g^{-1})	941.67	1112.11	1212.50	1180.06
V_T (cm^3 g^{-1})	0.56	0.63	0.69	0.68
V_m (cm^3 g^{-1})	0.28	0.29	0.28	0.29
S_m (m^2 g^{-1})	550.34	599.15	613.97	610.32
A_{ps} (nm)	2.36	2.25	2.26	2.31

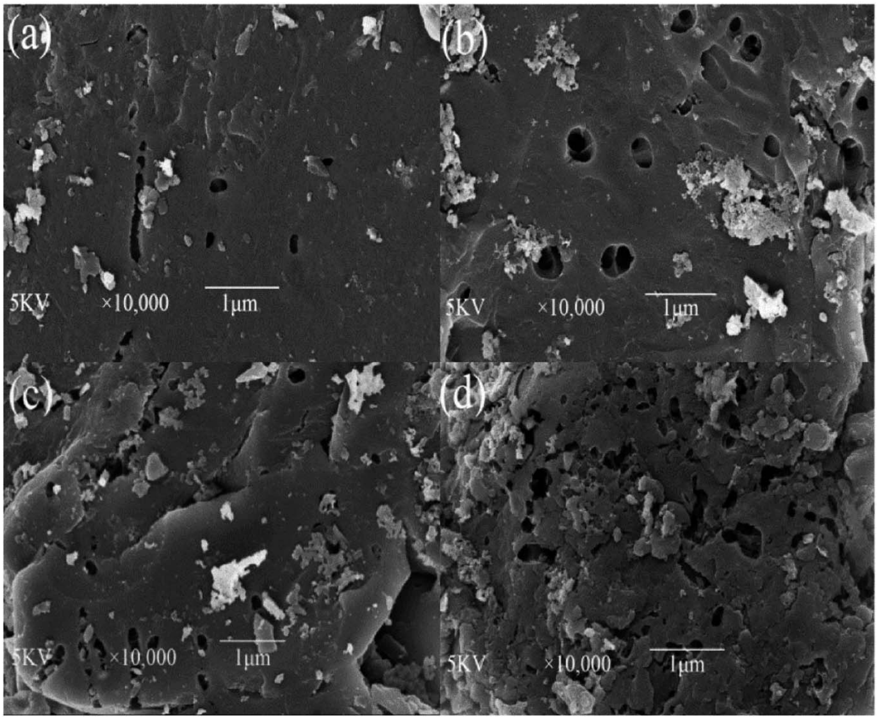

Fig. 7 SEM micrographs of (a) YLC-AC-1, (b) YLC-AC-2, (c) YLC-AC-3, (d) YLC-AC-4 selected at 10 000× magnification.

of CAR, the YLC-AC with different CAR were characterized by SEM, XRD and N_2 adsorption–desorption.

3.2.1. Porous structure analysis. The N_2 adsorption–desorption isotherms and pore size distribution of YLC-AC were shown in Fig. 6. The sorption isotherms of all samples show remarkable hysteresis at $P/P_0 > 0.4$, corresponding to the major mesopore distribution centered at 2–4 nm. According to the IUPAC classification, all samples exhibit type IV isotherms, indicating the presence of mesopores in materials.[32]

The effect of CAR on pore structure of CACs is shown in Table 5. The S_{BET} ($\mathrm{m^2\ g^{-1}}$) and V_{T} ($\mathrm{cm^3\ g^{-1}}$) increased with increasing CAR from 1 : 1 to 1 : 3. And YLC-AC-3 demonstrated a well-developed porosity with a surface area of 1212.50 $\mathrm{m^2\ g^{-1}}$ and a total volume of 0.69 $\mathrm{cm^3\ g^{-1}}$. When the CAR increased from 1 : 1 to 1 : 3, the S_{BET} and V_{T} of CACs increased simultaneously from 941.67 $\mathrm{m^2\ g^{-1}}$ to 1212.50 $\mathrm{m^2\ g^{-1}}$ and 0.56 $\mathrm{cm^3\ g^{-1}}$ to 0.69 $\mathrm{cm^3\ g^{-1}}$. The S_{BET} and V_{T} of YLC-AC-4 decreased when the CAR reached 1 : 4.

3.2.2. Surface morphology analysis. SEM images of the YLC-AC are shown in Fig. 7. After KOH activation, irregular surface with pores is observed on the obtained YLC-AC. The external surface of the YLC-AC-3 demonstrated a well pronounced pore structure than that of YLC-AC-1, YLC-AC-2 and YLC-AC-4, because the addition of KOH could enhance the pore development and create new pores during activation process.

3.2.3. Crystal structure. XRD patterns of the YLC and YLC-AC are shown in Fig. 8. No obvious diffraction peak is observed on YLC. All the YLC-AC samples shows an obvious peaks at around 26°, attributed to the (002) reflections of the layered carbon structure (JCPDS no. 41-1487). The peaks at around 44° on YLC-AC-1, YLC-AC-2 and YLC-AC-4 could be attributed to the (100) reflections of disordered stacking of micrographites. An obvious peak at around 29° on YLC-AC-3 is the (002) reflections of the disordered stacking of micrographites.[11]

CACs with high surface areas are generally used for dyes adsorption because of their excellent efficiency. Table 6 summarized the adsorption capacity of MB on different CACs. The YLC-AC-3 prepared in this study showed a better adsorption capacity of MB than most reported CACs. To further investigated the adsorption behavior of YLC-AC-3, the adsorption kinetics and isotherm models were studied.

3.3. Kinetics study of MB onto YLC-AC-3

To evaluate the adsorption behavior of MB on the surface of the YLC-AC-3, the experimental data at various contact time

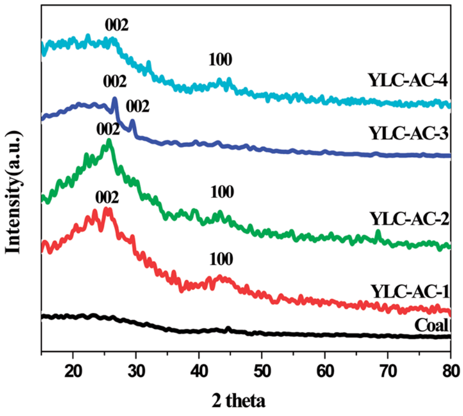

Fig. 8 XRD spectra of YLC, YLC-AC-1, YLC-AC-2, YLC-AC-3 and YLC-AC-4.

Table 6 Comparison of adsorption capacity of MB on different CACs

Adsorbents	Adsorption capacity (mg g^{-1})	Temperature (°C)	Initial concentration (mg L^{-1})	Dosage (g L^{-1})	References
Low-ranked lignite coal-based activated carbon	61.3	30	50	0.5	21
Thermal regeneration of spent coal-based activated carbon	365.26	25	400	1	33
Microwave assisted regeneration of spent coal based activated carbon	380.39	25	400	1	34
Bituminous coal-based activated carbon	580	20	800	1	13
Xinjiang–Kuche mine coal-based magnetic activated carbon	871	25	200	0.2	14
YLC-AC-3	547.35	25	550	1	This work

Table 7 R^2 and constant values for the different adsorption kinetic models

Kinetic Models	Parameters	YLC-AC-3
Pseudo-first order	R^2	0.7061
	$q_{e,cal}$ (mg g^{-1})	290.56
	k_1 (min^{-1})	0.0407
Pseudo-second order	R^2	0.9999
	$q_{e,cal}$ (mg g^{-1})	549.45
	k_2 (g mg^{-1} min^{-1})	0.00182
Intra-particle	R^2	0.9985
	k_{id1} (mg g^{-1} min$^{-1/2}$)	54.35
	R^2	0.8723
	k_{id2} (mg g^{-1} min$^{-1/2}$)	1.220
	R^2	0.9982
	k_{id3} (mg g^{-1} min$^{-1/2}$)	0.00249
Elovich	R^2	0.5889
	β (g mg^{-1})	0.04293

corresponding to adsorption amount of MB were fitted to four different kinetic models, including (i) pseudo-first order, (ii) pseudo-second order, (iii) intraparticle diffusion and (iv) Elovich models. They could be represented by the following equations.[35]

$$\ln(Q_e - Q_t) = \ln Q_e - K_1 t \tag{7}$$

$$\frac{t}{Q_t} = \frac{1}{K_2 {Q_e}^2} + \frac{t}{Q_e} \tag{8}$$

$$Q_t = K_t t^{1/2} + C \tag{9}$$

$$Q_t = \frac{1}{\beta}\ln(\alpha\beta) + \frac{1}{\beta}\ln t \tag{10}$$

Kinetic models are used to examine the rate of the adsorption process and potential rate determining step, *i.e.*, particle diffusion or chemical reaction.[36] Theoretically, the pseudo-first order model assumes that the adsorption rate of dye uptake with time is directly proportional to the difference between amount of dye absorbed with time and amount of dye absorbed at equilibrium. The pseudo-second order model is based on the assumption that chemisorption is the model's rate-limiting step, and the adsorption mechanism depends on the adsorbate and adsorbent involving valence forces through the sharing or exchange of electrons.[37,38] The intraparticle diffusion model is used to investigate rate controlling step during adsorption. The Elovich model is based on the assumption that the adsorption sites of the adsorbent are heterogeneous and displays a variety of activation energy during the adsorption process.[39] The R^2 and constant values were calculated and summarized in Table 7. Compared with other adsorption kinetic models, the R^2 value for the pseudo-second order kinetic

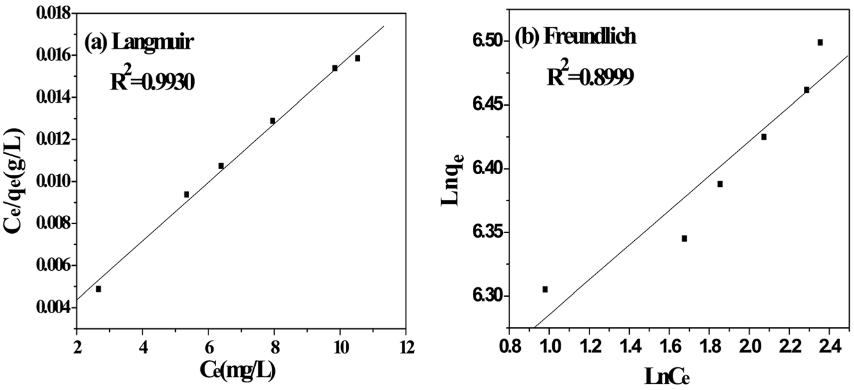

Fig. 9 Fitting plots of (a) Langmuir isotherm and (b) Freundlich isotherm models for MB onto the YLC-AC-3.

Table 8 R^2 and constant values for the different isotherm models

Models	Langmuir		Freundlich	
R^2	0.9930		0.8999	
Constant values	$q_{\max}$ (mg g^{-1})	714.29	$1/n$	0.136
	K_L (L mg^{-1})	0.886	K_F (L mg^{-1})	468.48

model is 0.9999 and the q_e value (amount of dye adsorbed at equilibrium) was 549.45 mg g^{-1} which was close to that of experimental value (547.35 mg g^{-1}), indicating the adsorption of MB onto the YLC-AC-3 follows the pseudo-second order kinetic model well.

3.4. Adsorption isotherms study of MB onto YLC-AC-3

The adsorption isotherms are used to define characteristic of the adsorption process between liquid and solid phases at equilibrium state. The most accepted surface adsorption models of single solute systems for analyzing experimental adsorption equilibrium data are the Langmuir and Freundlich model. Thus, the adsorption isotherm studies were carried out by varying the initial concentration of MB from 550 mg L^{-1} to 700 mg L^{-1} to obtain the adsorption equilibrium data.

3.4.1. Langmuir isotherm. The Langmuir isotherm model is based on the assumption that the adsorption process is a monolayer adsorption on a homogeneous adsorbent surface, there is no interaction between adsorbed molecules and the binding sites are finite and have the identical sorption energies.[40] The equation of Langmuir isotherm could be expressed as follows.

$$\frac{C_e}{Q_e} = \frac{C_e}{Q_m} + \frac{1}{K_L Q_m} \tag{11}$$

where C_e (mg L^{-1}) is dye concentration in liquid phase at equilibrium, Q_e (mg g^{-1}) is the equilibrium adsorption capacity, Q_m (mg g^{-1}) is the maximum amount of MB adsorbed and K_L (L mg^{-1}) is the Langmuir isotherm constant.

3.4.2. Freundlich isotherm. The Freundlich isotherm model assumes that the surface of adsorbent is heterogeneous in nature, regarding to the heat of adsorption.[41] The equation of Freundlich isotherm is expressed as follows.

$$\ln Q_e = \ln K_F + (1/n)\ln C_e \tag{12}$$

where Q_e (mg g^{-1}) represents the equilibrium adsorption capacity, C_e (mg L^{-1}) represents the equilibrium concentration, K_F (L mg^{-1}) is the Freundlich isotherm constant and $1/n$ is the value that decribe the heterogeneity of the adsorbent's surface.

Fig. 9 shows the plots of Langmuir and Freundlich isotherm models of MB onto the surface of YLC-AC-3. The value of R^2 for Langmuir isotherm model (0.9930) is much higher than that for Freundlich isotherm model (0.8999), indicating a better linearity. The adsorption process of MB onto the YLC-AC-3 follows the Langmuir isotherm model with the maximum monolayer adsorption amount of 714.29 mg g^{-1}. This result indicates that MB molecules may form monolayer coverage on the YLC-AC-3 (Table 8).

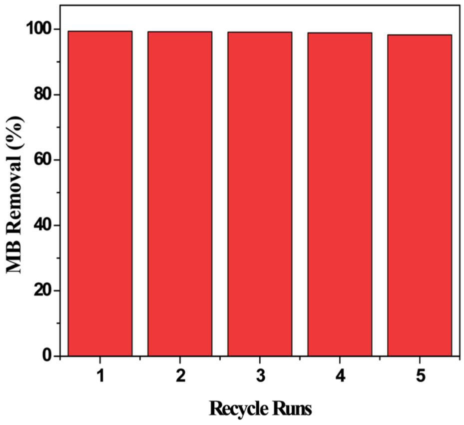

Fig. 10 The regeneration performance of the YLC-AC-3 for MB.

3.5. Regeneration performance

The regeneration of YLC-AC-3 was conducted up to five times. The results are shown in Fig. 10. The removal efficiency was 99.37% and 99.21% in the first two runs and decreased slightly to 98.87% and 98.21% in the fourth and fifth runs, respectively.

4. Conclusions

In this study, three kinds of coal with different ash and volatile matter content were chosen to prepare CACs. YLC-AC shows the better adsorption capacity of MB due to the high ash and volatile matter content in YLC. The effect of CAR on MB adsorption amount was also investigated. YLC-AC-3 exhibited a higher adsorption amount than other CACs due to the large surface area and pore volume. The adsorption kinetics of MB onto YLC-AC-3 was better described using a pseudo-second order model, it's proposed that the rate-limiting step is chemisorption. The adsorption behaviors fitted well to Langmuir isotherm model, the calculated adsorption capacity for MB is 714.29 mg g^{-1}. And the removal efficiency remains 98.21% after five runs. Current study shows that CACs prepared by coal with high ash and volatile matter content could be a promising raw material in fast removal of MB from wastewater.

Conflicts of interest

There are no conflicts to declare.

Acknowledgements

This research was supported by the National Natural Science Foundation of China (Grant 21376004) and the Shaanxi Provincial Science and Technology Program (Grant 12JK0577).

References

1 J. Z. Guo, B. Li, L. Liu and K. Lv, *Chemosphere*, 2014, **111**, 225–231.

2 S. C. Santos, V. J. Vilar and R. A. Boaventura, *J. Hazard. Mater.*, 2008, **153**, 999–1008.

3 T. Robinson, G. Mcmullan, R. Marchant and P. Nigam, *Bioresour. Technol.*, 2001, **77**, 247–255.

4 T. H. Liu, Y. H. Li, Q. J. Du, J. K. Sun, Y. Q. Jiao, G. M. Yang, Z. H. Wang, Y. Z. Xia, W. Zhang, K. L. Wang, H. W. Zhu and D. H. Wu, *Colloids Surf., B*, 2012, **90**, 197–203.

5 Y. Liu, J. J. Li, Y. Yang and B. P. Li, *Appl. Surf. Sci.*, 2015, **351**, 831–839.

6 D. Pathania, S. Sharma and P. Singh, *Arabian J. Chem.*, 2017, **10**, S1445–S1451.

7 M. A. M. Salleh, D. K. Mahmoud, A. W. A. K. Wan and A. Idris, *Desalination*, 2011, **280**, 1–13.

8 Ö. Gerçel, A. Özcan, A. S. Özcan and H. F. Gerçel, *Appl. Surf. Sci.*, 2007, **253**, 4843–4852.

9 G. Karaçetin, S. Sivrikaya and M. Imamoğlu, *J. Anal. Appl. Pyrolysis*, 2014, **110**, 270–276.

10 Y. Y. Sun, H. Li, G. C. Li, B. Y. Gao, Q. Y. Yue and X. B. Li, *Bioresour. Technol.*, 2016, **217**, 239–244.

11 X. M. Xiao, D. D. Liu, Y. J. Yan, Z. L. Wu, Z. S. Wu and G. Cravotto, *J. Taiwan Inst. Chem. Eng.*, 2015, **53**, 160–167.

12 T. Kopac and A. Toprak, *Int. J. Hydrogen Energy*, 2007, **32**, 5005–5014.

13 E. N. El Qada, S. J. Allen and G. M. Walker, *Chem. Eng. J.*, 2006, **124**, 103–110.

14 S. S. Gao, L. Liu, Y. K. Tang, D. Z. Jia, Z. B. Zhao and Y. Y. Wang, *J. Porous Mater.*, 2016, **23**, 877–884.

15 X. H. Duan, C. Srinivasakannan and J. S. Liang, *J. Taiwan Inst. Chem. Eng.*, 2014, **45**, 1618–1627.

16 D. Q. Li, X. F. Ma, J. Y. Yan, Z. S. Wu and Z. Y. Liu, *J. Chem. Soc. Pak.*, 2015, **37**, 1088–1098.

17 B. Jibril, R. S. Al-Maamari, O. Houache, M. Al-Aamri and A. M. Al-Qalhati, *J. Appl. Sci. Res.*, 2007, **3**, 1343–1351.

18 Y. Gao, S. P. Xu, Q. Y. Yue, Y. W. Wu and B. Y. Gao, *J. Taiwan Inst. Chem. Eng.*, 2016, **61**, 327–335.

19 T. Kopac, E. Sulu and A. Toprak, *Desalin. Water Treat.*, 2016, **57**, 29007–29018.

20 C. L. Lu, S. P. Xu, Y. X. Gan, S. Q. Liu and C. H. Liu, *Carbon*, 2005, **43**, 2295–2301.

21 B. Purevsuren, Y. H. Liou, Y. Davaajav, A. Ariunaa, S. Batbileg, B. Avid, S. Jargalmaa, Y. Huang and C. J. Lin, *J. Chin. Inst. Eng.*, 2017, **40**, 355–360.

22 M. C. Tellez-Juárez, V. Fierro, W. Zhao, N. Fernández-Huerta, M. T. Izquierdo, E. Reguera and A. Celzard, *Int. J. Hydrogen Energy*, 2014, **39**, 4996–5002.

23 D. D. Liu, Z. S. Wu, X. Y. Ge, G. Cravotto, Z. L. Wu and Y. J. Yan, *J. Taiwan Inst. Chem. Eng.*, 2016, **59**, 563–568.

24 C. Pelekani and V. L. Snoeyink, *Carbon*, 2000, **38**, 1423–1436.

25 M. J. Ahmed and S. K. Theydan, *J. Anal. Appl. Pyrolysis*, 2014, **105**, 199–208.

26 Y. B. Tang, Q. Liu and F. Y. Chen, *Chem. Eng. J.*, 2012, **203**, 19–24.

27 G. Z. Gong, Q. Xie, Y. F. Zheng, S. F. Ye and Y. F. Chen, *New Carbon Materials*, 2009, **24**, 141–146.

28 D. Cuhadaroglu and O. A. Uygun, *Afr. J. Biotechnol.*, 2008, **7**, 3703–3710.

29 F. C. Wu, P. H. Wu, R. L. Tseng and R. S. Juang, *J. Environ. Manage.*, 2010, **91**, 1097–1102.

30 W. Li, L. B. Zhang, J. H. Peng, N. Li and X. Y. Zhu, *Ind. Crops Prod.*, 2008, **27**, 341–347.

31 K. Y. Foo and B. H. Hameed, *Chem. Eng. J.*, 2012, **184**, 57–65.

32 W. G. Li, X. J. Gong, K. Wang, X. R. Zhang and W. B. Fan, *Bioresour. Technol.*, 2014, **165**, 166–173.

33 X. H. Duan, C. S. Kannan, W. W. Qu, X. Wang, J. H. Peng, L. B. Zhang and H. Y. Xia, *Color. Technol.*, 2012, **128**, 464–472.

34 X. H. Duan, C. Srinivasakannan, W. W. Qu, X. Wang, J. H. Peng and L. B. Zhang, *Chem. Eng. Process.*, 2012, **53**, 53–62.

35 T. Maneerung, J. Liew, Y. J. Dai, S. Kawi, C. Chong and C. H. Wang, *Bioresour. Technol.*, 2016, **200**, 350–359.

36 X. M. Xiao, F. Tian, Y. J. Yan, Z. L. Wu, Z. S. Zhan and G. Cravotto, *Korean J. Chem. Eng.*, 2015, **32**, 1129–1136.

37 F. Marrakchi, M. Auta, W. A. Khanday and B. H. Hameed, *Powder Technol.*, 2017, **321**, 428–434.

38 W. Konicki, A. Hełminiak, W. Arabczyk and E. Mijowska, *Chem. Eng. Res. Des.*, 2018, **129**, 259–270.

39 B. Acevedo, C. Barriocanal, I. Lupul and G. Gryglewicz, *Fuel*, 2015, **151**, 83–90.

40 L. Meng, X. F. Zhang, Y. S. Tang, K. H. Su and J. Kong, *Sci. Rep.*, 2015, **5**, 7910–7926.

41 M. Ghaedi, A. G. Nasab, S. Khodadoust, M. Rajabi and S. Azizian, *J. Ind. Eng. Chem.*, 2014, **20**, 2317–2324.